

Internal waves and turbulence in a stable stratified jet

HIEU T. PHAM AND SUTANU SARKAR†

Mechanical and Aerospace Engineering, University of California, San Diego, La Jolla, CA 92093, USA

(Received 17 April 2009; revised 15 October 2009; accepted 31 October 2009)

Direct numerical simulations are performed to investigate the interaction between a stably stratified jet and internal gravity waves from an adjacent shear layer with mild stratification. Results from two simulations are presented: one with the jet located far from the shear layer (far jet) and the other with the shear layer right on top of the jet (near jet). The near jet problem is motivated by velocity and stratification profiles observed in equatorial undercurrents. In the far case, internal waves excited by the Kelvin–Helmholtz (K-H) rollers do not penetrate the jet. They are reflected and trapped in the region between the shear layer and the jet and lead to little dissipation. In the near case, internal waves with wavelength larger than that of the K-H rollers are found in and below the jet. Pockets of hot fluid, associated with horseshoe vortices that originate from the shear layer, penetrate into the jet region, initiate turbulence and disrupt the internal wave field. Coherent patches of enhanced dissipation moving with the mean velocity are observed. The dissipation in the stably stratified near jet is large, up to three orders of magnitude stronger than that in the propagating wave field or the jet of the far case.

1. Introduction

The excitation of shear instability, i.e. Kelvin–Helmholtz (K-H) rollers, and its subsequent nonlinear evolution is one important source of turbulence and mixing in the stratified natural environment. Linear theory gives $Ri_g = N^2/S^2 < 0.25$, where Ri_g is the gradient Richardson number, N is the buoyancy frequency and S is the shear in the vertical direction, as a necessary condition for shear instability. The evolution of an unstable shear flow between two layers of homogeneous fluid with different density has been well studied using both laboratory experiments and numerical simulations (e.g. Thorpe 1973; Koop & Browand 1979; Smyth & Moum 2000; Caulfield & Peltier 2000; Brucker & Sarkar 2007). If one of the layers has continuous stratification, it can support propagating internal waves and also influence the evolution of the shear-layer instability as described in the studies of Sutherland & Linden (1998), Strang & Fernando (2001), Tse *et al.* (2003), Mahalov *et al.* (2007) and Pham, Sarkar & Brucker (2009). For instance, Pham *et al.* (2009) in their three-dimensional direct numerical simulation (DNS) study find that the wave energy flux is a significant fraction of the turbulent production and dissipation rate, suggesting that internal waves provide an important route of fluctuation energy from shear instabilities to the ocean interior. In the papers cited above, the waves are excited and propagate in a stratified background with no shear. However, in geophysical flows, the unstable stratified region is often

† Email address for correspondence: ssarkar@ucsd.edu

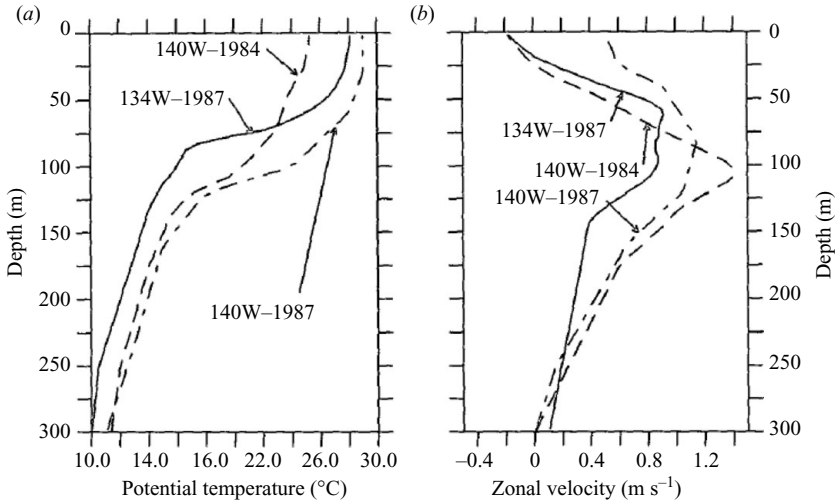


FIGURE 1. Typical temperature profile (a) and zonal currents (b) in the EUC system (Skillingstad & Denbo 1994).

adjacent to a stratified background with shear that is stable ($Ri_g > 0.25$). The objective of the current work is to characterize and understand the internal wave field and turbulent mixing in a nominally stable sheared region by simulation of a simple model problem: a stable jet adjacent to an unstable shear layer.

Equatorial undercurrents (EUC) provide an important example where internal waves and turbulence have been observed in a region of stable shear contiguous to a small region of unstable shear as described by Gregg *et al.* (1985), Peters, Gregg & Toole (1988), Moum *et al.* (1992) and Lien, McPhaden & Gregg (1996). The EUC are eastward jet-like flows below wind-driven westward surface currents. Typical temperature and streamwise velocity profiles are shown in figure 1. Internal waves are observed in the EUC and believed to be related to the enhanced deep-cycle turbulence in the upper flank of the EUC jet. The peak night time dissipation rate of the turbulent kinetic energy (TKE) in the marginally stable region exceeds the corresponding day time value by at least a factor of 10 (Moum *et al.* 1992; Lien *et al.* 1996). Hebert *et al.* (1992) capture a wave packet that is gravitationally unstable resulting in wave breaking. The dissipation rate within the patch of the overturning wave was found to be at least three orders of magnitude larger than outside the patch. Skillingstad & Denbo (1994) used two-dimensional non-hydrostatic simulations with the background profiles shown in figure 1 with forcing of wind stress and a heat flux at the surface. In the model, internal wave packets were observed to propagate downward and upstream relative to the jet velocity and the waves were shown to correlate with K-H instabilities. Sun, Smyth & Moum (1998) performed linear stability analysis using the hourly averaged current and stratification profiles and, from the computed positive growth rates in the regions with $Ri_g < 0.25$, inferred a connection between deep-cycle turbulence and shear instability.

Turbulence and internal waves in a stratified jet have been studied previously. Tse *et al.* (2003) use three-dimensional DNS to simulate a forced jet in quasi-equilibrium modelling of the tropopause jet. The buoyancy frequency in the upper flank of the jet is taken to be twice that in the lower flank. The jet, maintained at low Ri_g , is unstable. Turbulence is observed in the jet core while patchy turbulence and nonlinear evanescent waves are seen at the edges. Mahalov *et al.* (2007) investigate a similar

tropopause jet in a much larger domain than that used by Tse *et al.* (2003) by using numerical viscosity for the unresolved scales. Internal waves propagating into the region above the jet with stronger stratification are observed and characterized. Sutherland (2006) also models the tropopause jet but uses a piece-wise linear shear profile so that the upper flank of the jet is locally unstable while the lower flank is strongly stratified. Internal waves radiated from the upper flank are found to carry significant momentum into the region above the jet. Waves also propagate downward into the lower flank where they encounter a critical layer. Smyth & Moum (2002) employ linear stability analysis and two-dimensional DNS to study a Bickley jet that has a weak stratification in all of the upper flank and a strong stratification in the lower flank. They find that internal waves, generated by the dynamic instability of the weakly stratified upper flank, propagate downward and break upon encountering the critical level present at the more strongly stratified lower flank. Turbulence due to interaction between propagating waves and mean shear at a critical layer where the wave phase speed and the mean velocity is equal has been studied by Winters & D'Asaro (1994). In our model problem, a critical layer is absent by design.

Different from the three-dimensional simulations of Tse *et al.* (2003) and Mahalov *et al.* (2007) where the entire jet is unstable ($Ri_g < 0.25$) and the two-dimensional simulations of Smyth & Moum (2002) and Sutherland (2006) where a large portion of the jet is unstable, we use three-dimensional DNS to investigate internal waves and turbulence inside a stable jet ($Ri_g > 0.25$) located adjacent to an unstable shear layer. Our set-up has the feature of a stratified stable jet contiguous to an unstable shear layer in common with the EUC but is simplified by the absence of wind forcing and diurnal cycle of heat flux. Our objectives are to provide a better understanding of some dynamical processes related to EUC mixing by answering the following questions in the model problem: (i) Can internal waves excited from an adjacent region of unstable shear propagate downward into a stably stratified jet? (ii) Is there significant dissipation in the jet despite its stable stratification? (iii) What is the connection between the propagating internal waves and turbulence in the jet?

2. Model formulation

The flow corresponds to a weakly stratified shear layer situated on top of a strongly stratified jet. A schematic is given in figure 2. The shear layer has a hyperbolic tangent profile with velocity difference ΔU ,

$$\langle u_s \rangle = -\frac{\Delta U}{2} \tanh\left(\frac{2z}{\delta_{\omega,0}}\right),$$

where the initial vorticity thickness is defined by $\delta_{\omega,0} = \Delta U / (d\langle u_s \rangle / dz)_{max}$. The angled brackets denote a x - y plane average.

A jet with peak velocity $2\Delta U$ and half-width $3\delta_{\omega,0}$ is added to the region below the shear layer and has the following profile:

$$\langle u_j \rangle = 2\Delta U \exp\left[-\left(\frac{z - D_j}{3\delta_{\omega,0}}\right)^4\right],$$

where D_j is the distance between the shear-layer centre and the jet centre. The complete velocity profile consists of the shear layer and the jet, $\langle u \rangle(z) = \langle u_s \rangle(z) + \langle u_j \rangle(z)$. Using the squared buoyancy frequency defined as $N^2(z) = -(g/\rho_0) d\langle \rho \rangle / dz$, the stratification is described with a non-dimensional Richardson number,

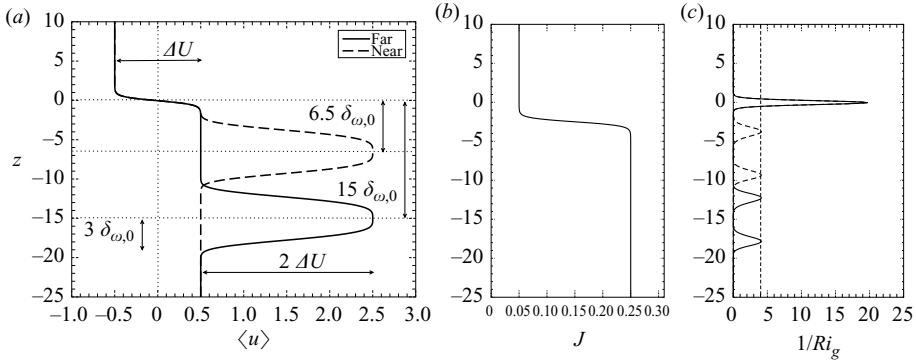


FIGURE 2. (a) Initial mean profiles. The velocity profile corresponds to a shear layer on top of a jet. The jet centre is at depth $z = -15 \delta_{\omega,0}$ in the *far jet* and at depth $z = -6.5 \delta_{\omega,0}$ in the *near jet*. (b) Initial stratification profiles $J(z)$ are used in both cases. (c) Initial $1/Ri_g(z)$ profiles.

$J(z) = N^2(z) \delta_{\omega,0}^2 / \Delta U^2$. The initial stratification in the shear layer is $J_s = 0.05$ whereas at $z = -2.5\delta_{\omega,0}$ the stratification transitions to $J_j = 0.25$ in the deep jet region. The complete initial stratification profile is given by

$$J(z) = \frac{J_s + J_j}{2} + \frac{J_s - J_j}{2} \tanh\left(\frac{z + 2.5\delta_{\omega,0}}{0.5\delta_{\omega,0}}\right).$$

The stratification is chosen such that the gradient Richardson number Ri_g shown in figure 2(c) corresponds to field measurement in the EUC system. Peters *et al.* (1988) report three vertical regions of the EUC jet: (i) the upper shear zone, from 23 m to 100 m below the ocean surface, has low Ri_g , average of 0.35; (ii) the core, between 100 m and 130 m, has $Ri_g > 2$; and (iii) the lower shear zone, below 130 m, has $Ri_g \approx 0.5$. In our model, the jet has constant stratification such that the initial Ri_g in the upper shear region is approximately 0.25 slightly less than the value 0.35 reported in the field data. The smaller value is taken because Ri_g in this region approaches the field value, because of viscous effects, by the time the unstable shear layer has fully developed K-H rollers.

The initial shear-layer vorticity thickness $\delta_{\omega,0}$, the density jump $\Delta\rho_0$ across twice the initial vorticity thickness and the velocity difference ΔU are used for non-dimensionalization. We solve the Navier–Stokes equations under the Boussinesq approximation:

$$\frac{\partial u_k}{\partial x_k} = 0, \quad (2.1)$$

$$\frac{\partial u_i}{\partial t} + \frac{\partial (u_k u_i)}{\partial x_k} = -\frac{\partial p}{\partial x_i} + \frac{1}{Re_0} \frac{\partial^2 u_i}{\partial x_k \partial x_k} - Ri_{b,0} \rho' \delta_{i3}, \quad (2.2)$$

$$\frac{\partial \rho}{\partial t} + \frac{\partial (u_k \rho)}{\partial x_k} = \frac{1}{Re_0 Pr} \frac{\partial^2 \rho}{\partial x_k \partial x_k}. \quad (2.3)$$

The non-dimensional parameters are Reynolds number $Re_0 = \Delta U \delta_{\omega,0} / \nu$, Prandtl number $Pr = \nu / \kappa$ and bulk Richardson number $Ri_{b,0} = (g \Delta \rho_0 \delta_{\omega,0}) / (\rho_0 \Delta U^2)$. Here, ν is the kinematic viscosity and κ is the molecular diffusivity. Two simulations are performed with varying jet distance: $D_j = 6.5\delta_{\omega,0}$ (near jet) and $15\delta_{\omega,0}$ (far jet). Both simulations are run with $Re_0 = 1280$, $Pr = 1$ and $Ri_{b,0} = 0.1$. The near jet models the

typical velocity profile of the EUC system while the far jet has a shear-free region with distinct internal wave propagation that helps understand the more complex physics in the near jet.

The initial velocity perturbations (u' , v' , w') have an amplitude of 0.1% ΔU and a broadband spectrum given by

$$E(k) \propto k^4 \exp \left[-2 \left(\frac{k}{k_0} \right)^2 \right],$$

where k_0 is set such that the spectrum peaks at $1.7\delta_{\omega,0}$.

Periodic boundary conditions are used in the streamwise (x) and spanwise (y) directions. Boundary conditions in the vertical direction (z) are set as follows:

$$\begin{aligned} u(z_{min}) &= \frac{1}{2}, & u(z_{max}) &= -\frac{1}{2}, \\ v(z_{min}) &= v(z_{max}) = 0, \\ p(z_{min}) &= p(z_{max}) = 0, \\ \frac{\partial w}{\partial z}(z_{min}) &= \frac{\partial w}{\partial z}(z_{max}) = 0, \\ \frac{\partial \rho}{\partial z}(z_{max}) &= -\frac{J_s}{g}, \\ \frac{\partial \rho}{\partial z}(z_{min}) &= -\frac{J_j}{g}. \end{aligned}$$

The domain size is $50.4\delta_{\omega,0} \times 16.8\delta_{\omega,0} \times 55.0\delta_{\omega,0}$ and the grid has $384 \times 128 \times 512$ points. The grid is uniform in the horizontal with spacing of $0.13125\delta_{\omega,0}$. The vertical grid size is $0.075\delta_{\omega,0}$ in the region $-19 < z < 3.5\delta_{\omega,0}$. Outside this region, the grid is mildly stretched at 2%. A second-order finite-difference method on a staggered grid is used for spatial derivatives and a third-order low storage Runge–Kutta method is used for time advancement.

A sponge region is employed at the top ($z > 12\delta_{\omega,0}$) and the bottom ($z < -26\delta_{\omega,0}$) boundaries to eliminate wave reflections. The velocities and density in this sponge region are relaxed by adding to the right-hand side of (2.2) and (2.3) a term of the form

$$\begin{aligned} & -\phi(z) [u_i(x_i, t) - \langle u \rangle_i(z, t = 0)], \\ & -\phi(z) [\rho(x_i, t) - \langle \rho \rangle(z, t = 0)]. \end{aligned}$$

The damping function, $\phi(z)$, increases quadratically from $\phi = 0$ to 1.0.

The evolution of the shear layer includes shear instability, formation of the K-H rollers and their breakdown into small-scale three-dimensional turbulence. Simulations are continued until most of the fluctuations are dissipated, roughly at $t_f = 350$ time units ($\delta_{\omega,0}/\Delta U$). Details of the numerical methods can be found in Basak & Sarkar (2006), Brucker & Sarkar (2007) and Pham *et al.* (2009).

3. Far jet

As the shear layer evolves, K-H rollers form and excite waves. The waves behave linearly similar to the ones analysed in our previous work (Pham *et al.* 2009). Nonetheless, there are inherent differences because of the presence of the jet, a

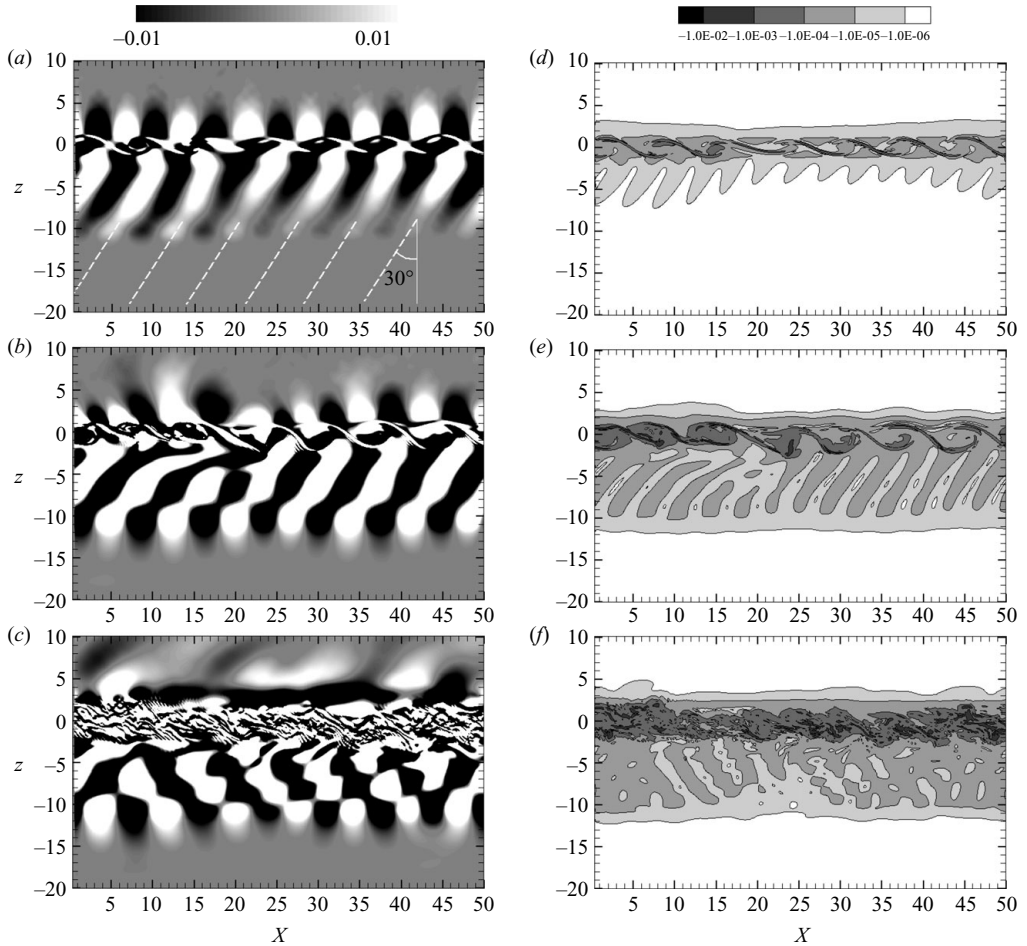


FIGURE 3. Far jet. Instantaneous wave field in the x - z plane at $y=8.4\delta_{\omega,0}$: (a) $\partial w'/\partial z$ at $t=100$; (b) $\partial w'/\partial z$ at $t=150$; (c) $\partial w'/\partial z$ at $t=200$; (d) ε at $t=100$; (e) ε at $t=150$; (f) ε at $t=200$. Dashed lines in (a) indicate propagation angle predicted by linear wave theory.

feature that was absent in Pham *et al.* (2009). In this section, we examine the wave characteristics as well as their role in the TKE budget.

3.1. Internal wave field

Figure 3(a-c) gives the visualization of the wave field through the instantaneous fields of $\partial w'/\partial z$ at different times $t=100, 150$ and 200 . The coherent lines of constant phase in figure 3(a) are parallel to the wave group velocity and are inclined at an angle of 28° - 34° to the vertical. Later, when the waves enter the jet region, approximately at $z=-10\delta_{\omega,0}$, they are restrained from penetrating the jet and are reflected back towards the shear layer as shown in figure 3(b,c). The region between the shear layer and the jet has overlapping phase lines of the incident and reflected waves. Figure 3(d-f) shows the turbulent dissipation, ε , at corresponding times; these are discussed later in the text.

The waves shown in figure 3(a) are observed to lock onto the K-H instability mode. They have horizontal wavenumber $k\delta_{\omega,0}=0.87$ according to figure 4(a), corresponding to horizontal wavelength $\lambda_h=7.2\delta_{\omega,0}$, which is equal to the wavelength of the most

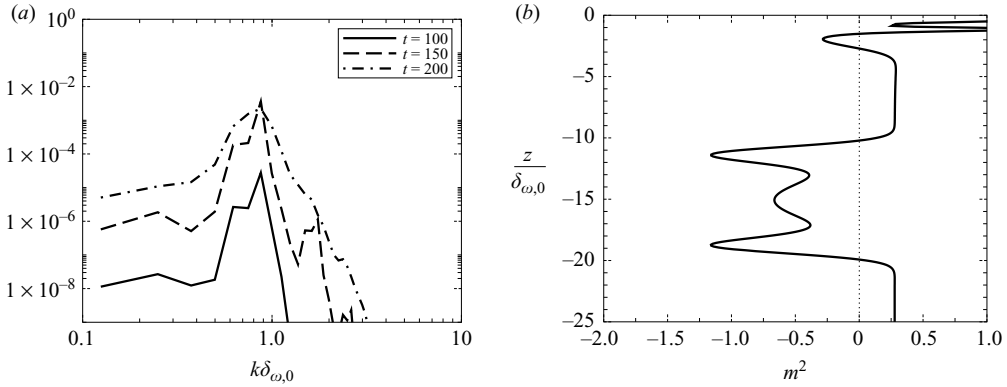


FIGURE 4. Far jet. (a) Horizontally averaged power spectra of the vertical velocity w on the horizontal plane $z = -10\delta_{\omega,0}$ at various times. (b) Squared vertical wavenumber m^2 at $t = 100$ computed using $k\delta_{\omega,0} = 0.87$ and $c_a = 0$.

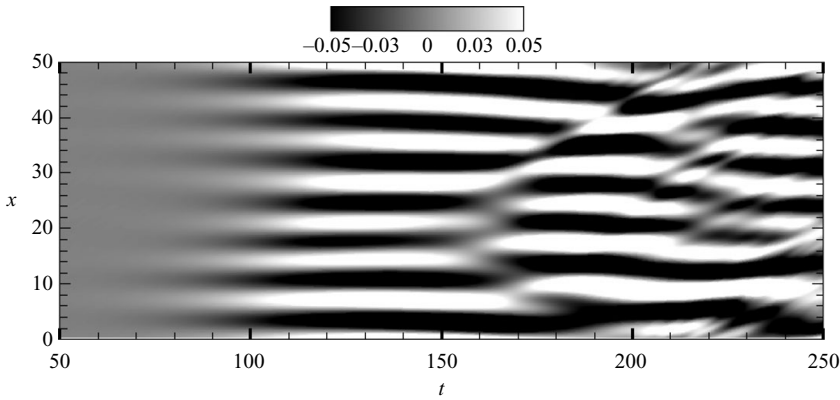


FIGURE 5. Far jet. Instantaneous w field in the $x-t$ plane at $y = 8.4\delta_{\omega,0}$ and $z = -6\delta_{\omega,0}$.

unstable mode, equivalently the spacing between K-H rollers in the shear layer. The $x-t$ diagram of the vertical velocity field w at $y = 8.4\delta_{\omega,0}$ and $z = -6\delta_{\omega,0}$ in figure 5 indicates the waves are stationary in the simulated frame during the time period between $t = 75$ and 150 . Therefore, the apparent phase speed of the wave is $c_a = 0$. Between $t = 150$ and 200 , the waves are still stationary but exhibit a phase shift. The positive wave crests (white) become negative troughs (black) and vice versa. Beyond $t = 200$, waves with shorter wavelength and non-zero phase speed are also present, being excited by smaller-scale turbulence in the shear layer.

The waves excited by the K-H rollers exhibit linear behaviour and, therefore, the propagating angle can be predicted by linear wave theory. In the simulation frame, the K-H rollers have zero convective velocity $\langle u \rangle = 0$ while the convective velocity is $\langle u \rangle = 0.5\Delta U$ in the region between the shear layer and the jet. This set-up resembles the problem of a flow of constant velocity over stationary surface corrugations that can be solved explicitly. Owing to a Doppler shift, the wave intrinsic speed in the region between the shear layer and the jet is $c_i = c_a + 0.5\Delta U = 0.5\Delta U$ giving the wave intrinsic frequency $\Omega = c_i k = 0.435\Delta U/\delta_{\omega,0}$. Linear wave theory predicts that Ω relates to the ambient stratification N by $\Omega = N \cos \theta$, where θ is the angle between the wave phase line and the vertical. Note that θ is computed to be 30° using

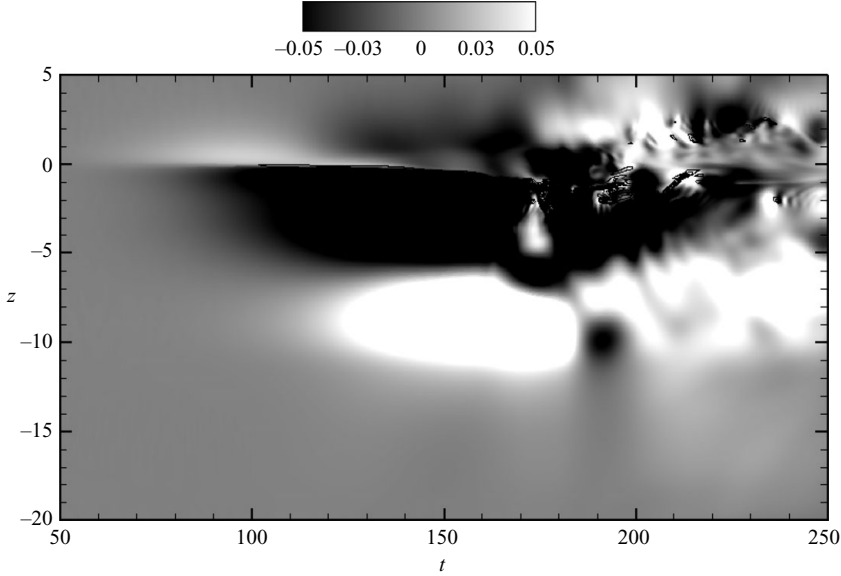


FIGURE 6. Far jet. Instantaneous w field in the z - t plane at $x = 25.2\delta_{\omega,0}$ and $y = 8.4\delta_{\omega,0}$.

$N = \sqrt{J_j} = 0.5$. The numerical value predicted by linear wave theory agrees well with the visualization shown in figure 3(a).

Since the vertical direction is non-periodic in our simulation, we cannot directly compute the vertical wavenumber m using a Fourier transform. Nonetheless, we can estimate m using the Taylor–Goldstein (T-G) equation that follows from linear theory:

$$\frac{d^2 w}{dz^2} + m^2 w = 0, \quad (3.1)$$

where,

$$m^2 = \frac{N^2}{(c_a - \langle u \rangle)^2} + \frac{d^2 \langle u \rangle / dz^2}{(c_a - \langle u \rangle)} - k^2.$$

The squared vertical wavenumber m^2 is a key determinant of wave properties: when $m^2 > 0$, the solution consists of propagating modes and, in contrast, the waves are evanescent when $m^2 < 0$. The vertical profile of m^2 , calculated using its definition in the T-G equation and plotted in figure 4(b), shows that the region between the shear layer and the jet allows wave propagation since $m^2 > 0$. The vertical wavenumber is computed to be $m \approx 0.5\delta_{\omega,0}^{-1}$ giving a vertical wavelength $\lambda_v \approx 12.6\delta_{\omega,0}$, which is longer than the distance between the shear layer and the top edge of the jet (the far jet starts at $z = -10\delta_{\omega,0}$). The z - t diagram of the vertical velocity field w at $x = 25.2\delta_{\omega,0}$ and $y = 8.4\delta_{\omega,0}$ in figure 6 can be used to substantiate the vertical wavenumber m predicted by linear wave theory. Prior to $t = 150$, the waves are stationary with a distinct trough with negative (black) velocity and a positive (white) crest. The vertical extent of the wave trough is approximately $6\delta_{\omega,0}$, which is comparable with half of the vertical wavelength λ_v predicted by linear wave theory. It is noted that the vertical extent of the trough is longer than that of the crest below it, since the propagating region $m^2 > 0$ between the shear layer and the jet is less than one complete wavelength as shown in figure 4(b).

Figure 4(b) also shows that the jet region $-10 < z < -20\delta_{\omega,0}$ has $m^2 < 0$ and thus the waves in this region are evanescent with an amplitude that decays sharply with depth. This agrees well with the visualization in figures 3(b,c) and 6, suggesting the applicability of linear theory to characterize K-H-excited internal waves in this problem.

3.2. Turbulent kinetic energy budget

The evolution equation for the turbulent kinetic energy is

$$\frac{dK}{dt} = P - \varepsilon + B - \frac{\partial T_i}{\partial x_i}. \quad (3.2)$$

Here, K is the turbulent kinetic energy defined as $K = 1/2\langle u'_i u'_i \rangle$, P is the production rate, defined as

$$P \equiv -\langle u'_i u'_j \rangle \frac{\partial \langle u_i \rangle}{\partial x_j} = -\langle u' w' \rangle \frac{d\langle u \rangle}{dz},$$

ε is the dissipation rate, defined as

$$\varepsilon \equiv \frac{2}{Re_0} \langle s'_{ij} s'_{ij} \rangle; s'_{ij} = \frac{1}{2} \left(\frac{\partial u'_i}{\partial x_j} + \frac{\partial u'_j}{\partial x_i} \right),$$

B is the buoyancy flux, defined as

$$B \equiv -\frac{g}{\rho_0} \langle \rho' w' \rangle,$$

$\partial T_i / \partial x_i$ is the transport of *tke*, defined as

$$T_i \equiv \frac{1}{2} \langle u'_i u'_j u'_j \rangle + \langle u'_i p' \rangle / \rho_0 - \frac{2}{Re_0} \langle u'_j s'_{ij} \rangle.$$

For the present flow, the transport term simplifies to $\partial T_3 / \partial z$ with

$$T_3 = T_t + T_p + T_v, \quad (3.3)$$

where the turbulent transport T_t is defined as

$$T_t = \frac{1}{2} [\langle w' u' u' \rangle + \langle w' v' v' \rangle + \langle w' w' w' \rangle],$$

the pressure transport T_p is defined as

$$T_p = \frac{\langle p' w' \rangle}{\rho_0},$$

and the viscous transport T_v is

$$T_v = -\frac{2}{Re_0} [\langle u' s'_{31} \rangle + \langle v' s'_{32} \rangle + \langle w' s'_{33} \rangle].$$

Since the current problem involves both internal waves and turbulence, *TKE* and K are understood to be ‘fluctuating’ kinetic energy comprised of energy because of both waves and turbulence.

We now examine the role of the internal waves in the evolution of *TKE*. The terms in the *TKE* budget are shown in figure 7(a) at $t = 118$. When the K-H rollers are present in the shear layer, *TKE* is extracted from the mean velocity leading to the production P . The buoyancy flux B in the shear layer is significant because the rollers are large-scale, two-dimensional structures capable of entraining the heavier fluid

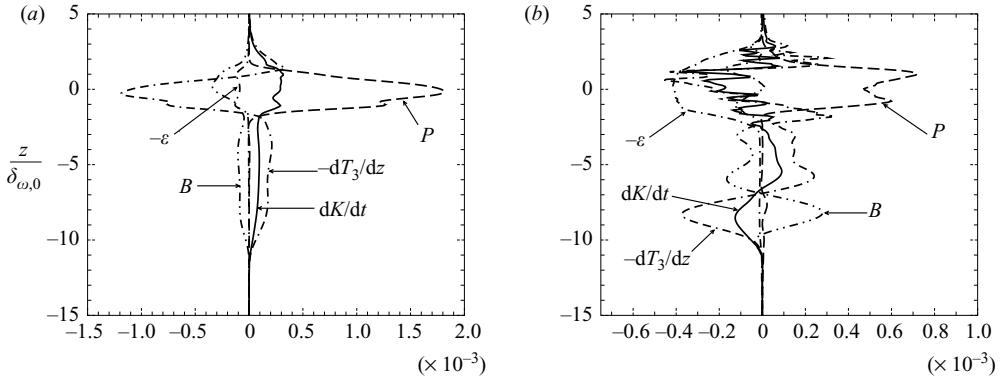


FIGURE 7. Far jet. *TKE* budget at (a) $t = 118$ and (b) $t = 183$.

from the bottom region into the shear layer. Owing to the lack of three-dimensional fine scales at this time, the turbulent dissipation, ε , in the shear layer is somewhat smaller than B . While the production and the dissipation rate are limited in extent to the shear layer, the buoyancy flux, the transport dT_3/dz and the transient term dK/dt extend far into the bottom region reaching the top edge of the jet at $z \approx -10\delta_{\omega,0}$. Thus, the signature of internal waves propagating in a stratified shear-free background can be seen in the *TKE* budget through non-zero values of dK/dT , dT_3/dz and B . Since there is no background shear, internal waves do not lead to production of *TKE* and they are substantially less dissipative than the perturbations inside the shear layer. All terms in the *TKE* budget rapidly decrease to zero in the jet region below $z = -10\delta_{\omega,0}$ because the internal waves are evanescent in this region as discussed above. Although the jet has background shear, there is neither jet instability nor shear production because the jet is strongly stratified ($Ri_g > 0.25$ in the jet). Linear inviscid wave theory states that internal waves exhibit energy equipartition, i.e. half of the energy carried by the waves is fluctuating kinetic energy *TKE* while the other half is in fluctuating potential energy *TPE* defined as $TPE = (g^2 \langle \rho'^2 \rangle) / (2\rho_0 N^2)$. The negative of the buoyancy flux, $-B$, is equal to the rate of change of *TPE* which, because of equipartition, is equal to the rate of change in turbulent kinetic energy, dK/dt , and inserting $B = -dK/dt$ in the *TKE* equation leads to the total rate of *TKE* transport, $-dT_3/dz = 2dK/dt$. The waves in the region $-3 < z < -10\delta_{\omega,0}$ in figure 7(a) approximately follow this property of linear inviscid waves in a shear-free background.

At $t = 183$, the shear layer is turbulent with the dissipation as a significant term of the *TKE* budget as shown in figure 7(b). At this time, the region between the shear layer and jet has waves that propagate both upward and downward. Again, the production and the dissipation in this region outside the shear layer are significantly smaller than the other terms. The instantaneous dissipation field ε shown in figure 3(d–f) further emphasizes that ε is large solely in the shear layer. The wave propagation region between the shear layer and the jet has substantially lower ε , at least three orders of magnitude less than the peak value in the shear layer.

We now discuss the transport term T_3 in (3.3), which redistributes fluctuation energy in physical space. Integration of (3.2) across the region of interest from depth $z^* = -5\delta_{\omega,0}$ to z_{max} , the maximum vertical location in the test domain (excluding the

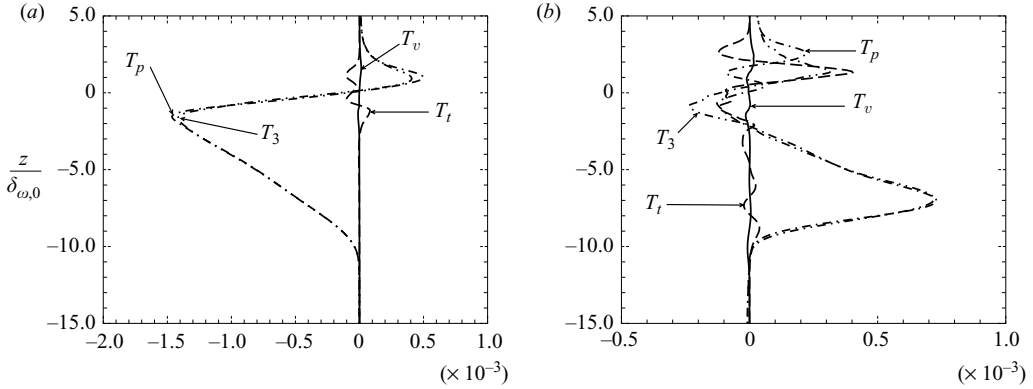


FIGURE 8. Far jet. Components of transport T_3 at (a) $t = 118$ and (b) $t = 183$.

sponge region), we obtain

$$\int_{z^*}^{z_{max}} \frac{dK}{dt} dz = \int_{z^*}^{z_{max}} P dz - \int_{z^*}^{z_{max}} \varepsilon dz + \int_{z^*}^{z_{max}} B dz + T_3(z^*). \quad (3.4)$$

Note that T_3 at z_{max} is found to be zero. Equation (3.4) indicates that the rate of change of TKE in the region of interest is influenced by the rate of TKE transport, T_3 , across the lower boundary $z = z^*$. According to (3.3), the total transport T_3 has three contributions: turbulent T_t , pressure T_p and viscous T_v . Figure 8(a,b) shows profiles of T_3 and its components. At $t = 118$, when the K-H rollers are dominant, T_p is the largest component of the total transport. T_v is substantially smaller while T_t is significant only in the shear layer. In the region $-10 < z < -3\delta_{\omega,0}$, all the TKE transport comes from pressure transport consistent with the picture that linear internal waves are responsible for the transport of fluctuation energy to the region external to the shear layer. Figure 8(b), corresponding to a time when the shear layer is turbulent, shows that T_t extends down to $z = -10\delta_{\omega,0}$, a larger depth than at $t = 118$. Note that T_t in the region $-10z < -3\delta_{\omega,0}$ has alternating signs inferring small-amplitude high-frequency internal waves excited by turbulent shear layer. Nevertheless, T_p dominates the total transport. Furthermore, T_p is positive, changing sign with respect to $t = 118$, showing that internal waves reflected from the jet transport energy upward towards the shear layer. Thus, it is feasible to spatially differentiate a turbulent region from a region with propagating linear waves in the flow using the turbulent transport term; a turbulent region has both T_p and T_t comparably contributing to T_3 , while a wave region has a dominant contribution from T_p to T_3 .

To illustrate the significance of the TKE carried by the wave field, we track the evolution of TKE in two separate regions: one from z^* to z_{max} and the other over the entire test domain. The result is shown in figure 9(a), where the solid line indicates the integration of K over the test domain and the dashed line indicates the integration from z^* to z_{max} . The location of z^* is chosen to be $-5\delta_{\omega,0}$ because T_t at this depth is relatively small over the duration of the simulation. The difference between the solid and dashed lines corresponds to TKE in the region below the shear layer. Prior to $t = 100$, TKE is generated inside the shear layer and then transported into the region below z^* by internal waves. TKE is not transported into the region above the shear layer because this region does not support K-H-excited waves and turbulence-excited waves are significantly weaker in terms of energy transport (Pham *et al.* 2009). At $t = 170$, when TKE inside the shear layer reaches its maximum value, TKE carried

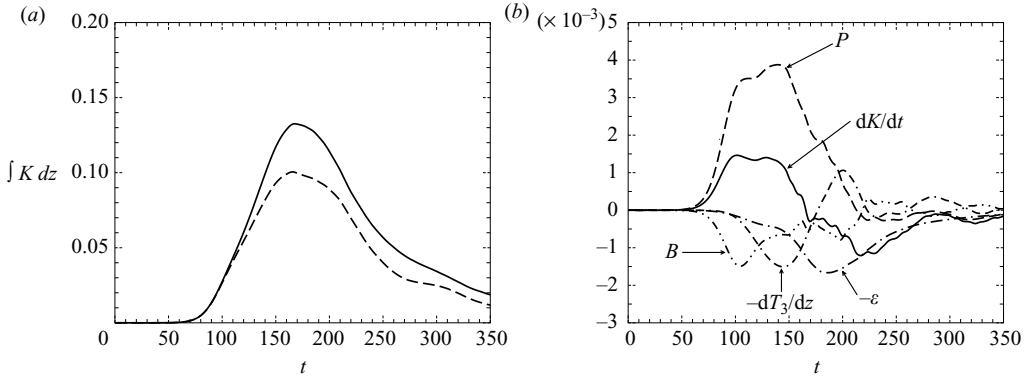


FIGURE 9. Far jet. (a) Dashed line represents integrated TKE from $z^* = -5\delta_{\omega,0}$ to z_{max} ; solid line represents integrated TKE across the test domain. (b) Terms in the TKE budget integrated from z^* to z_{max} .

by internal waves can be as large as 30% of the maximum value inside the shear layer. TKE is transported back into the shear layer between $t = 250$ and 300 , leading to a noticeable lessening of rate of TKE decay during that time interval.

The role of TKE transport by internal waves can be further quantified by tracking the time evolution of the terms indicated in (3.4) as shown in figure 9(b). The term dT_3/dz is spatially integrated instead of taking T_3 at z^* as in (3.4) although both provide the same results. In the figure, prior to $t = 180$ the transport term is negative, indicating that TKE is carried outside the shear layer. After that, it changes sign so that TKE is transported upward into the domain of integration. The peak value of the transport is as large as the peak values of the buoyancy flux and the dissipation in the current study and somewhat larger than the peak value of the transport reported by Pham *et al.* (2009), which was about 33% of the peak dissipation and 75% of the peak buoyancy flux. The difference between the two studies is due to the constructive interference between incident and reflected waves in the current investigation. Although energy carried by the internal waves is large compared with other terms in the integrated TKE budget, the wave energy is lost only because of the viscous dissipation, ε , whose structure was shown earlier in figure 3(d-f). The value of ε in the jet is small relative to that in the shear layer. There is no signature of induced ‘deep-cycle turbulence’ in the stratified jet that has been observed in the EUC system.

4. Near jet

The evolution of the fluctuations in the near case is significantly different from that in the far case. First, internal waves are observed in and below the jet. Second, ‘hot pockets’ of fluid are observed to penetrate into the cold jet region and are precursors to coherent patches of *strong* induced dissipation, much larger than in the far jet. Below, we elaborate on these remarks.

4.1. Internal wave field

Instantaneous fields of $\partial w'/\partial z$ are shown in figure 10(a,b) at time $t = 125$ – 150 to visualize the internal wave field. In figure 10(a), the wave phase lines are not clear in the jet region $-2.5 < z < -10\delta_{\omega,0}$, but there are four ellipse-shaped lobes in the vicinity of $z = -10\delta_{\omega,0}$ with alternating signs implying two crests and two troughs. In

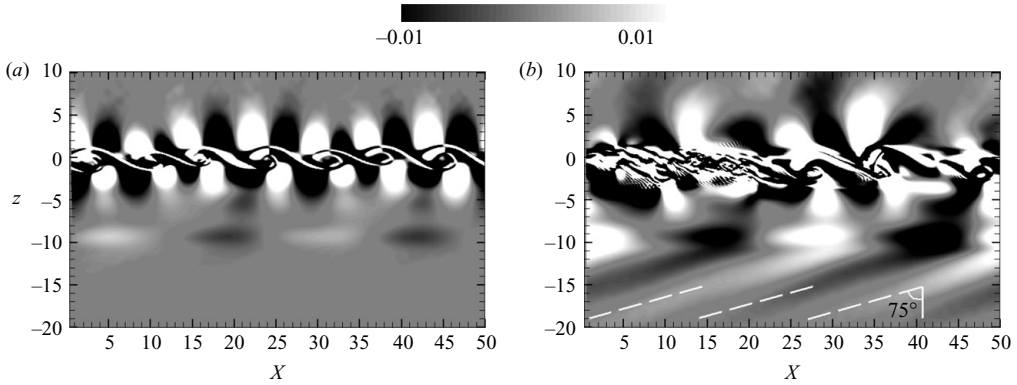


FIGURE 10. Near jet. Internal wave field is visualized through a slice of $\partial w'/\partial z$ in the x - z plane at $y = 8.4\delta_{\omega,0}$ at time (a) $t = 125$ and (b) $t = 150$.

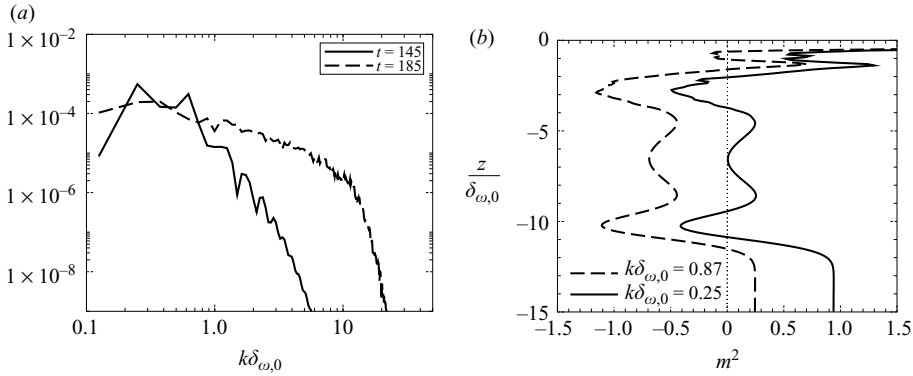


FIGURE 11. Near jet. (a) Horizontally averaged power spectra of the vertical velocity w on the horizontal plane $z = -4\delta_{\omega,0}$ at various times. (b) Squared vertical wavenumber m^2 at $t = 150$ computed using $c_a = 0$ and two values of horizontal wavenumber: $k\delta_{\omega,0} = 0.25$ based on the peak of energy spectrum at $t = 145$ in (a) and $k\delta_{\omega,0} = 0.87$ based on the K-H mode.

figure 10(b), phase lines which originate from the lobes are clear. The propagation angle θ is between 74° – 78° to the vertical. Waves of horizontal wavelength larger than that observed in the *far* case are excited by larger-wavelength disturbances in the shear layer that occur owing to the nonlinear interaction, including pairing of the K-H rollers.

The horizontally averaged power spectra of the vertical velocity w measured at $z = -4\delta_{\omega,0}$, a location outside the shear layer, are shown in figure 11(a). The spectrum at $t = 145$ shows a distinct peak at $k\delta_{\omega,0} = 0.25$, implying that waves are not excited by K-H-rollers but rather by smaller-wavenumber disturbance in the shear layer. The contour plot of the vertical velocity w in the x - t plane at $y = 8.4\delta_{\omega,0}$ and $z = -4\delta_{\omega,0}$ shown in figure 12 further characterizes the internal waves in the jet. The x -wavelength increases from the K-H value after $t = 100$ to a wavelength approximately equal to $25\delta_{\omega,0}$, yielding the wavenumber $k\delta_{\omega,0} = 0.25$ in good agreement with the spectral peak shown in figure 11(a). Figure 12(b) shows the dissipation field corresponding to the field shown in figure 12(a) and will be discussed later.

Linear wave theory can be used to explain why the K-H rollers cannot excite internal waves. Profiles of m^2 , as defined in (3.1), are shown in figure 11(b) with

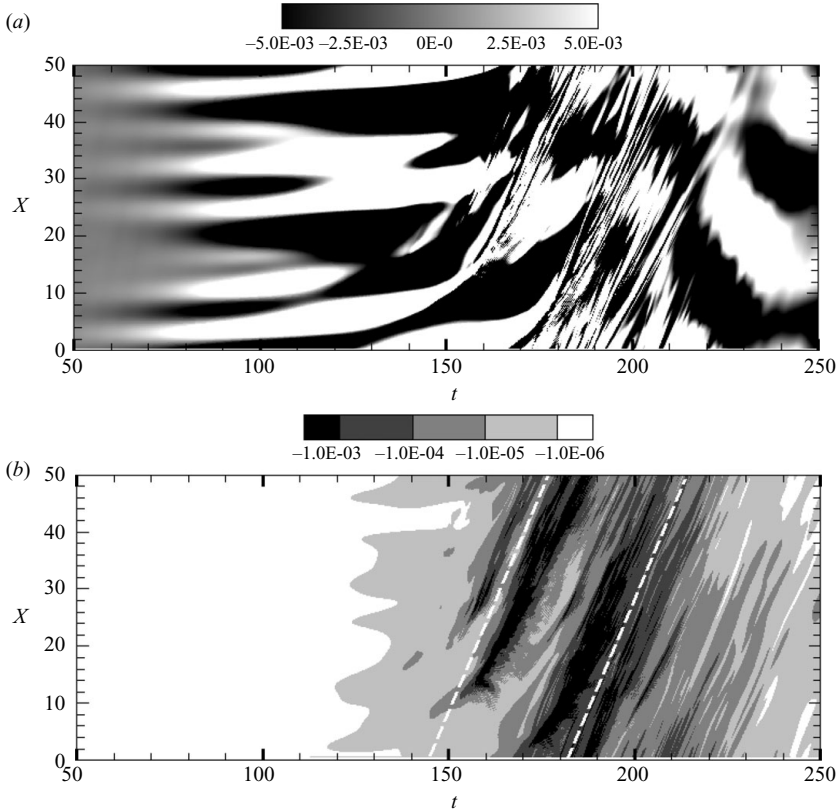


FIGURE 12. Near jet. (a) Instantaneous vertical velocity field w in the x - t plane at $y = 8.4\delta_{\omega,0}$ and $z = -4\delta_{\omega,0}$. (b) Instantaneous dissipation field ε on the same plane. The white dashed lines denote $\langle u \rangle = dx/dt \approx 1.7\Delta U$.

two different values of horizontal wavenumber $k\delta_{\omega,0} = 0.25$ and 0.87 . The former corresponds to the spectral peak in figure 11(a) and the latter is the wavenumber for K-H instability. Clearly, $m^2 < 0$ over the whole jet for $k\delta_{\omega,0} = 0.87$ and $m^2 > 0$ in the region $-4 > z > -9\delta_{\omega,0}$ of the jet for $k\delta_{\omega,0} = 0.25$. As a result, K-H-excited waves cannot propagate inside the jet. The four distinct lobes observed at $z \simeq -10\delta_{\omega,0}$ in figure 10(a,b) are consistent with the transition from $m^2 > 0$ to $m^2 < 0$ in the solid line of figure 11(b) at $z \simeq -10\delta_{\omega,0}$. The observation of lobes here is analogous to the lobes in the far case shown in figure 3(b) at $z = -10\delta_{\omega,0}$ where there is a similar change in the sign of m^2 . However, different from the far case, freely propagating waves are observed in the near jet below the evanescent region with $m^2 < 0$ because they can tunnel through the evanescent region, which is thinner relative to the far jet. Internal wave tunnelling through a stratified shear region is possible, for example, see Brown & Sutherland (2007).

The internal waves propagating in the region below the jet are observed to be linear, similar to those in the far case. The propagation angle θ can be predicted as in the previous section. Taking the apparent phase speed $c_a = 0$ gives the intrinsic phase speed in this region as $c_i = 0.5\Delta U$. With the horizontal wavenumber $k = 0.25\delta_{\omega,0}$, linear theory yields the intrinsic frequency $\Omega = 0.13\Delta U/\delta_{\omega,0}$ and propagation angle $\theta = 75^\circ$. This agrees well with the visualization given in figure 10(b). It is worth noting that, different from the studies of Smyth & Moum (2002) and Sutherland (2006),

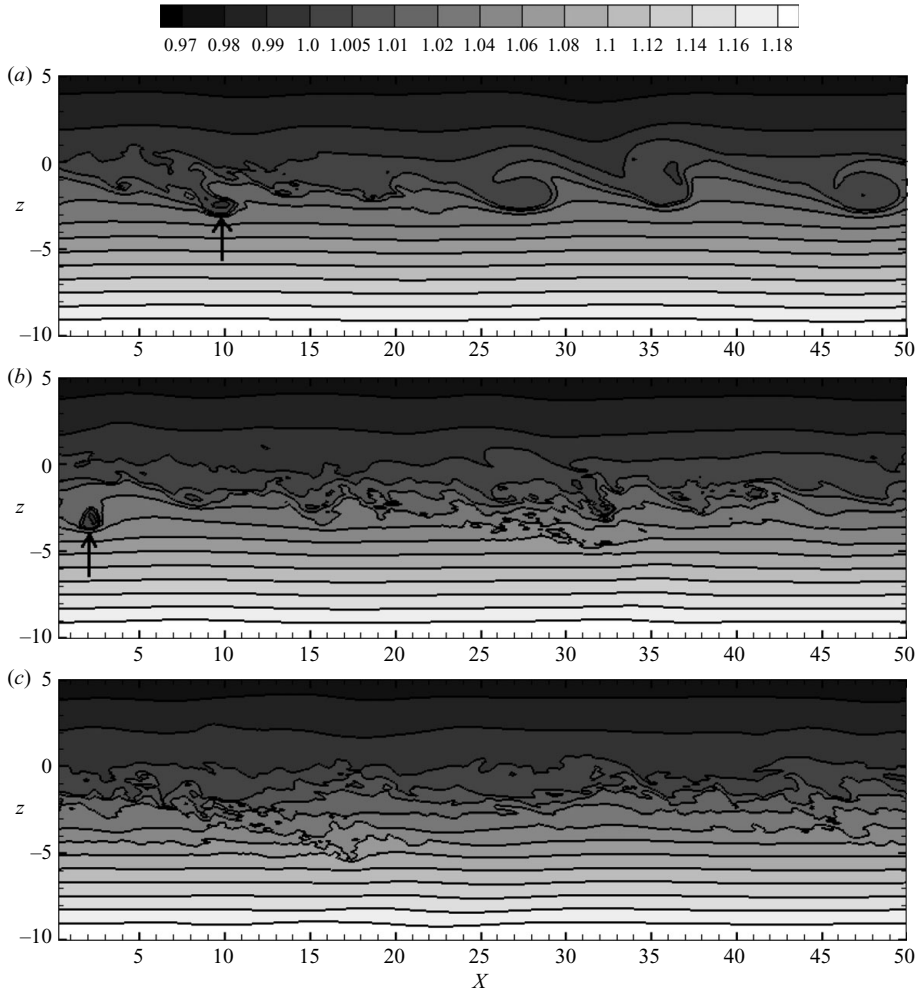


FIGURE 13. Near jet. Iso-contours in the density field in the x - z plane at $y = 8.4\delta_{\omega,0}$. (a-c) correspond to $t = 150, 170$ and 185 , respectively. Arrow indicates ‘hot pocket’.

a critical layer does not exist in our simulated jet. The observed waves have phase speed in the opposite direction of the jet such that there is no location at which the wave phase speed is equal to the free-stream velocity. The value of m^2 is finite in the jet as shown in figure 11(b) in contrast to a critical layer that would have an infinite value of m^2 .

4.2. ‘Hot pockets’

During the time between $t = 140$ and 200 , we observe distinct events of a ‘light’, equivalently ‘hot’, pocket of fluid entrained into the cold jet region as shown in figure 13 (a-c). The figure shows the density iso-contours in the vertical x - z plane at $y = 8.4\delta_{\omega,0}$ at various times. A ‘hot pocket’ is observed in the upper flank of the cold jet region at $x \approx 10\delta_{\omega,0}$ in figure 13(a). The pocket is swept downstream and stretched by the background jet shear. The fluctuations in the vicinity of the pocket gain intensity and their spatial extent increases. Figure 13(b) shows that, eventually, the region $-4 < z < -2\delta_{\omega,0}$ and $20 < x < 35\delta_{\omega,0}$ contains numerous small-scale structures

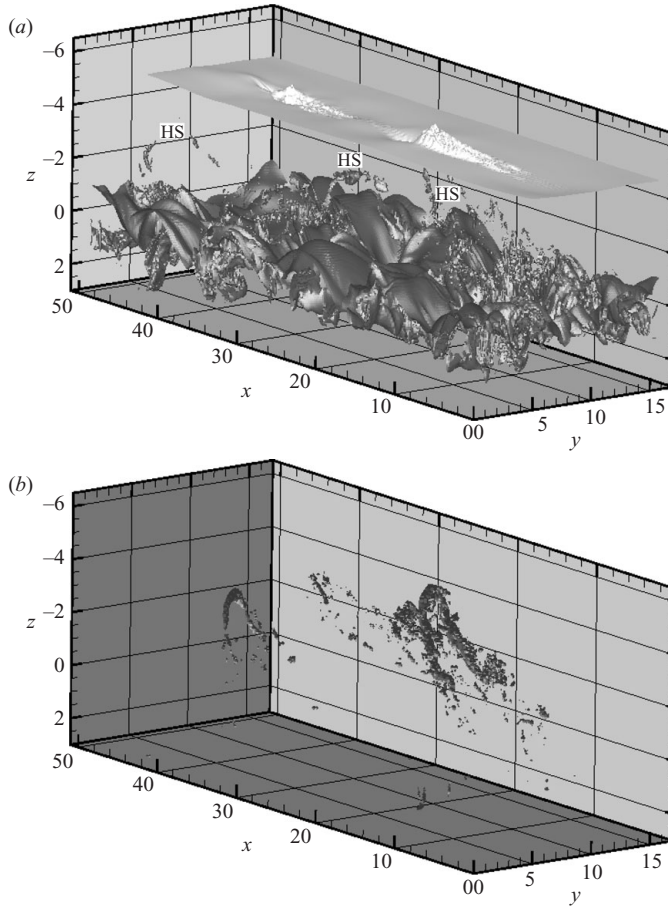


FIGURE 14. Three-dimensional structure of the ‘hot pockets’ in the near jet. Note that, for clearer visualization, the vertical coordinate is *flipped* with up in the figure representing down in physical space. (a) Isopycnal surfaces at $t = 162$: the darker isopycnal corresponds to $\rho = 1.0$, originally at $z = 0$ while the lighter isopycnal corresponds to $\rho = 1.07$, originally at $z = -4.7\delta_{\omega,0}$, near the centre of the jet. HS indicates horseshoe-like structures in the density field. (b) Isosurface of the quantity $\Delta = 5$ at $t = 162$ shows the horseshoe vortices that correspond to the HS structures in the density field shown in (a).

indicating turbulence activity. At $x \approx 2\delta_{\omega,0}$ in figure 13(b), there appears another ‘hot pocket’, which induces turbulence in the vicinity of $x \approx 15\delta_{\omega,0}$ later, as shown in figure 13(c). The ‘hot pocket’ also leads to fluctuations that penetrate into the deeper region, down to $z = -5\delta_{\omega,0}$. The horizontal extent of the fluctuation regions left by the pockets is similar in both the events and comparable to half the wavelength of the internal waves observed in figure 10(b).

Figure 14(a) provides the three-dimensional structure of these ‘hot pockets’. The HS symbols denote horseshoe-like density structures which, in two-dimensional cuts, appear as ‘hot pockets’. These structures originate from the shear layer where they are coherent and extend into the jet where they are mixed by their interaction with the background shear. The structure at $x \approx 15\delta_{\omega,0}$ penetrates deep into the jet core and impinges the isopycnal at that location causing a localized region of intense fluctuation. The density structures are associated with horseshoe vortices as shown in

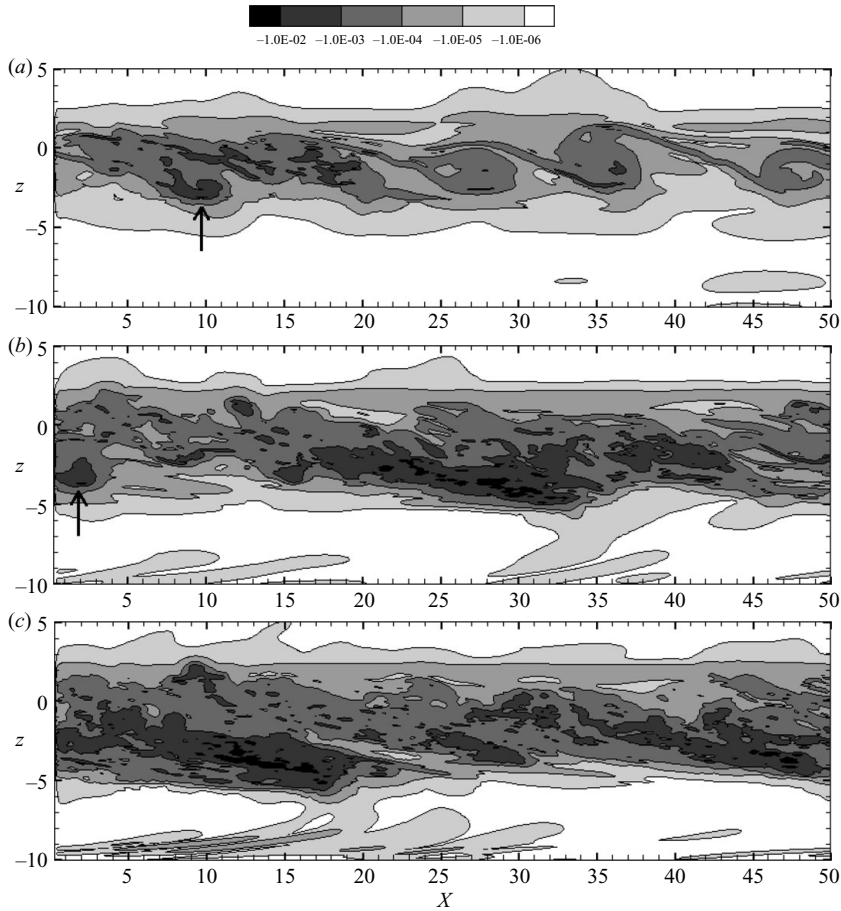


FIGURE 15. Near jet. Iso-contours in the dissipation field in the x - z plane at $y = 8.4\delta_{\omega,0}$. (a-c) correspond to $t = 150, 170$ and 185 , respectively. Arrow indicates 'hot pocket'.

figure 14(b). Here, a vortex structure is identified using the Δ criterion as in Jeong and Hussain (1995). As the horseshoe vortex penetrates into the jet, it is elongated owing to stretching by the background shear, the vorticity is intensified, and it is able to continue further into the jet despite the stable stratification. The vortex tube thins owing to its elongation until it is finally extinguished by molecular mixing.

4.3. Induced dissipation

Figure 15(a-c) illustrates the instantaneous dissipation field ε corresponding to the density field shown in figure 13(a-c), respectively. Clearly, the 'hot pockets' in figure 13(a-c) correlate with the coherent patches that have large dissipation in figure 15(a-c). The patch of turbulence that originates from the 'hot pocket' in figure 15(a) intensifies in figure 15(b), which coincides with the strong fluctuation regions shown in figure 13(b). At time $t = 185$, the dissipation in the upper flank of the jet is *stronger* than in the shear layer. The value of ε in the near jet has values up to three orders of magnitude larger than the dissipation in the wave propagation region of the far jet. These turbulence patches move with the free-stream velocity u as shown in the x - t diagram in figure 12(b). The patches with the strongest dissipation shown in black convect in the positive x direction with the slope dx/dt equal to the local

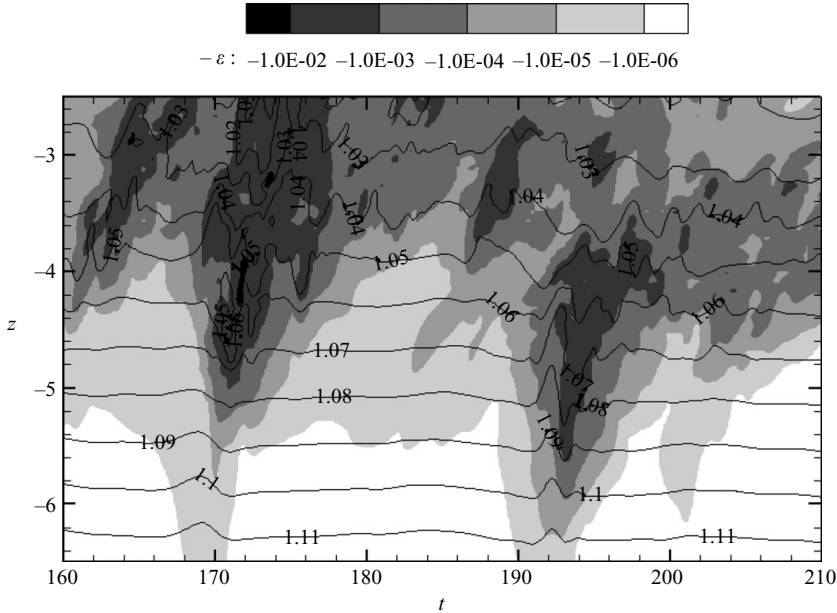


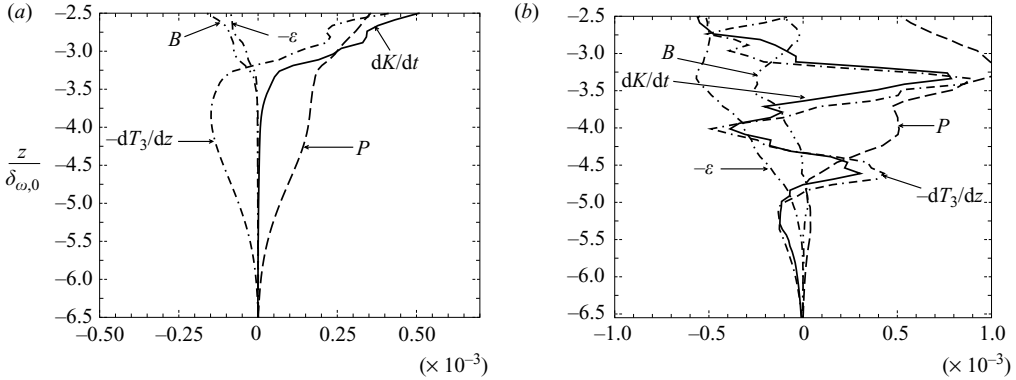
FIGURE 16. Near jet. Instantaneous dissipation field ϵ in the z - t plane at $x = 25.2\delta_{\omega,0}$ and $y = 8.4\delta_{\omega,0}$. Solid lines are isopycnals.

value of $\langle u \rangle$. Therefore, these patches have the apparent phase speed $c_a = \langle u \rangle$ moving downstream and thus intrinsic phase speed $c_i = 0$, in contrast to the internal waves shown by the contour plot of w field during the time $t = 100$ and 150 in figure 12(a) that have $c_a = 0$ and $c_i = \langle u \rangle$ moving upstream. The dissipation in the internal wave field prior to $t = 100$ in figure 12(b) is substantially smaller than that in the induced patches that occur later. The horizontally averaged power spectrum at $z = -4\delta_{\omega,0}$ and at time $t = 185$ shown in figure 11(a) indicates that the jet is broadband turbulent with no distinct peaks. The peaks seen in the spectrum at earlier time $t = 145$ prior to the ‘hot pocket’ penetration have disappeared.

Figure 16 shows a contour plot of the instantaneous dissipation field along with isopycnals in the z - t plane at $x = 25.2\delta_{\omega,0}$ and $y = 8.4\delta_{\omega,0}$. Two patches of induced turbulence are observed approximately at $t = 170$ and 191 . The latter penetrates to greater depth compared with the former. Both patches are accompanied by fluctuations in the isopycnals. To the left of the regions with strongest dissipation ($\epsilon > 10^{-3}$), high-amplitude low-frequency waves are observed, while to the right are low-amplitude high-frequency fluctuations. Distinct wavepackets are observed directly below the patches in the bottom three isopycnals. These packets are high-frequency disturbances with a lifetime small compared with the buoyancy time period.

4.4. Turbulent kinetic energy budget

As shown in the previous section, the penetration of the ‘hot pockets’ into the cold jet region starts the chain of events that culminates in patches of induced dissipation. The internal waves observed to propagate inside the jet disappear after the penetration. In this section, we analyse the *TKE* budget to elucidate the energy pathways that feed the dissipation patches. Figure 17(a,b) presents the *TKE* budgets at time $t = 143$ before the first ‘hot pocket’ begins to penetrate the jet and at $t = 171$ corresponding to figures 13(b) and 15(b) in which the induced dissipation in the jet is observed. When

FIGURE 17. Near jet. TKE budget at (a) $t = 143$ and (b) $t = 171$.

internal waves propagate in a quiescent background, the rate of energy transport dT_3/dz is equipartitioned between the time rate of change in the turbulent kinetic energy dK/dt and the buoyancy flux B as shown previously in the far case. In contrast, at time $t = 143$ the production P balances the transport dT_3/dz in the region from depth $z = -4\delta_{\omega,0}$ to the jet centre. The production in this region is different from that observed in the shear layer. The latter is the result of energy extraction from the unstable mean shear, namely turbulent production, while the former originates from the interaction between the momentum flux carried by the internal waves and the background stable jet shear, namely wave production. The dissipation ε is insignificant at $t = 143$, consistent with the low dissipation behaviour of the propagating internal waves shown in figure 12(b). The buoyancy flux B is relatively smaller than P and dT_3/dz because the effect of mean shear, which is involved in the definition of P and dT_3/dz , is stronger on P and T_3 than on B . Here, the TPE carried by the waves is less than the TKE, which is different from the far jet, where the TPE is equal to TKE. At time $t = 171$, in the region $-5.5 < z < -4.5\delta_{\omega,0}$, the buoyancy flux B changes sign and locally becomes a TKE source, a signature of counter-gradient heat flux. The available potential energy carried by the ‘hot pockets’ is released into kinetic form. Nonetheless, this energy source is significantly smaller than the energy lost to the induced dissipation.

To examine the role of the waves in the energy transport, the contributions to the transport term T_3 are analysed. As explained previously, the contributions are viscous diffusion T_v , turbulent transport T_t and pressure transport T_p . Figure 18(a,b) shows the contributions to the total transport at time $t = 143$ and 171, respectively. In figure 18(a), there are clearly two distinct regions: a wave-dominated region (below $z = -3.5\delta_{\omega,0}$) with little turbulence and a region with stronger turbulence (above $z = -3.5\delta_{\omega,0}$). T_p and T_3 are equal in the wave-dominated region, i.e. all the contribution to the transport is due to pressure. On the other hand, the transport in the turbulent region has significant contribution from T_t . The turbulent region $-3.5\delta_{\omega,0} < z < 0$ in figure 18(a) thickens to $-5\delta_{\omega,0} < z < 0$ in figure 18(b) as evidenced by the drop of T_p and the increase in T_t to become the dominant component of transport. In other words, part of the wave-dominated region in figure 18(a) becomes turbulence dominated in figure 18(b). The inference is that the internal wave field has evolved into turbulence.

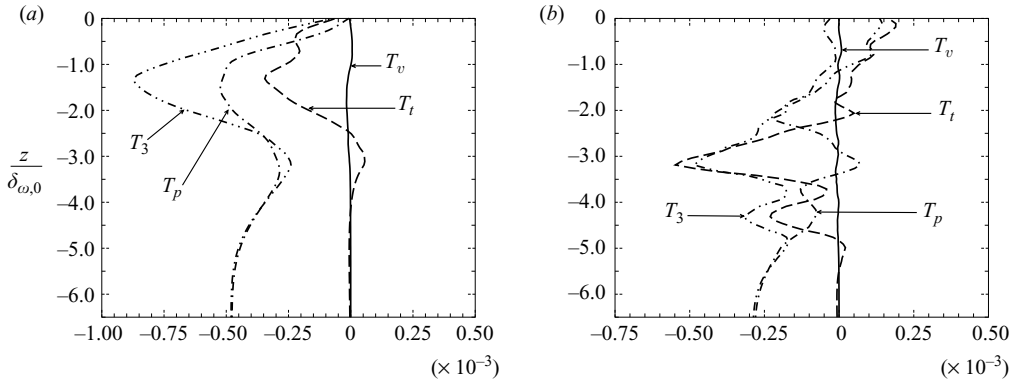


FIGURE 18. Near jet. Components of TKE transport T_3 at (a) $t = 143$ and (b) $t = 171$.

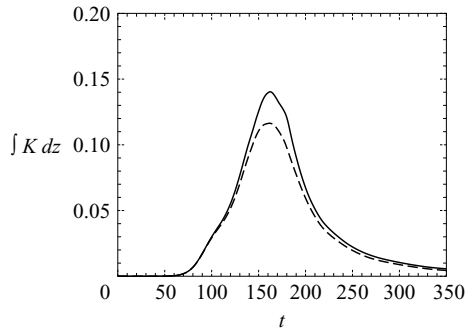


FIGURE 19. Near jet. The dashed line indicates integrated *TKE* in the region $-2.5 < z < z_{max}$. The solid line indicates integrated *TKE* over the entire test domain. The difference between the two lines is the *TKE* outside the shear layer and in the jet.

How large is the wave energy contribution to the *TKE* that resides in the jet and external to the shear layer? Figure 19 illustrates the time evolution of the integrated *TKE* over two spatial regions: one from $-2.5 < z < z_{max}$ shown by the dashed line and the other across the entire test domain shown by the solid line. The evolution consists of three significant periods of time. The first period is between $t = 100$ and 150 , when internal waves transport energy outside the shear layer. Figures 17(a) and 18(a) indicate that energy accumulation during this period is from wave production and wave transport. During the second period between $t = 150$ and 200 , there are significant fluctuations outside the shear layer which, being quickly dissipated over the period, is indicative of turbulence. The amount of energy accumulated inside the jet during the first period is smaller than the amount observed during the second period. Possible sources of energy accumulation in the jet are from the transport (both wave and turbulence), the production (both waves and turbulence) and counter-gradient buoyancy flux. As shown earlier, the counter-gradient heat flux is local and weak compared with other terms in the budget. The wave transport and wave production are too small to account for the larger *TKE* accumulation relative to that seen during the first period. This leaves turbulence transport and turbulent shear production as contributors to the large amount of energy observed during the time period $150 < t < 200$. It is worth noting that this is the time when the ‘hot pockets’ are active

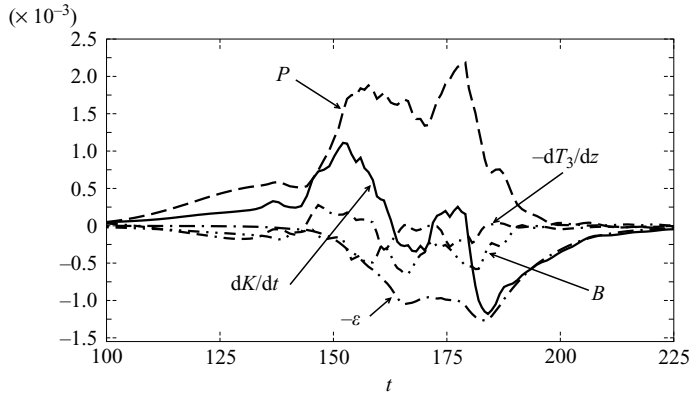


FIGURE 20. Near jet. Integrated TKE budget. The terms are spatially integrated in the jet upper flank $-6.5 < z < -2.5\delta_{\omega,0}$.

in the jet. In the third period, $t > 200$, there is a small difference between the two lines as in the first period.

The time evolution of the spatially integrated *TKE* budget is given in figure 20 to further elucidate the energy pathways leading to the enhanced *TKE* and dissipation in the near jet. The terms in the *TKE* budget are spatially integrated over the jet upper flank $-6.5 < z < -2.5\delta_{\omega,0}$. Before the penetration of the first ‘hot pocket’ at $t \approx 145$, there is no dissipation in the region. The transport is mostly from the pressure transport, T_p . Positive dK/dt indicates an accumulation of *TKE*, mainly due to the positive wave production associated with wave momentum flux $\langle u'w' \rangle$ interacting with the stable background shear. At $t \approx 145$, the ‘hot pocket’ penetrates the region causing the buoyancy flux to become less negative because of the positive effect of counter-gradient heat flux. The ‘hot pocket’ also arrives with turbulence transport T_t causing the transport term, $-dT_3/dz$, to become positive, i.e. a source of energy. Nonetheless, the largest source of *TKE* is the production. The production and the dissipation peak twice corresponding to the two ‘hot pocket’ penetrations. The overall evolution of the budget indicates that most of the *TKE* accumulated in the region is due to shear production by interaction with both internal waves and turbulence. The counter-gradient heat flux resulting from the ‘hot pockets’ can be a source locally in space; however, overall, the buoyancy flux is an energy sink. Integrating over time, the energy lost to the induced dissipation is mainly contributed by the production.

In this study, where both waves and turbulence are involved, it is not straightforward to identify when $\langle u'w' \rangle$ represents wave momentum flux and when it is due to turbulent Reynolds shear stress. One way to differentiate between the two is to perform a spectral analysis of the $u'w'$ field. The horizontally averaged co-spectrum measured at $z = -4\delta_{\omega,0}$ shown in figure 21 indicates that the peak value of the wave momentum flux (at $t = 145$) is an order of magnitude weaker than that of the Reynolds stress (at $t = 180$). The spectrum for the wave momentum flux clusters at low wavenumbers, while the turbulent Reynolds stress has a broadband spectrum. Thus, the time evolution of the integrated production P shown in figure 20 consists of two regimes: wave production prior to $t = 145$ and turbulence production during $t = 145$ and 200. The latter is significantly larger than the former.

The gradient Richardson profile $Ri_g(z)$, computed using horizontal averages of N and vertical shear S , which is plotted in figure 22 indicates that linear shear instability

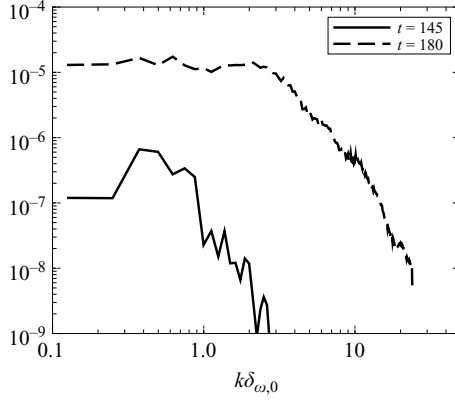


FIGURE 21. Near jet. Horizontally averaged power co-spectra of Reynolds stress $u'w'$ at $z = -4\delta_{\omega,0}$.

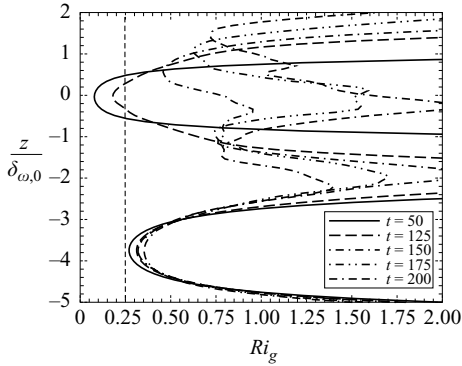


FIGURE 22. Near jet. Ri_g profiles.

in the jet is infeasible because $Ri_g(z) > 0.25$. At early time, the value of Ri_g is less than 0.25 only in the shear layer. The value of Ri_g at $z = -4\delta_{\omega,0}$ increases in time even when the ‘hot pockets’ are active. Nonetheless, the fields of local $\hat{R}i_g$, computed on the x - z plane at $y = 8.4\delta_{\omega,0}$ and shown in figure 23(a-c) at $t = 100, 150$ and 170 indicate the potential for local shear instability. Here, $\hat{R}i_g$ is defined as

$$\hat{R}i_g(x, y, z, t) = \frac{(-g/\rho_0)d\rho/dz}{(du/dz)^2},$$

where u and ρ are instantaneous values. In figure 23(a), there are three visible bands with low $\hat{R}i_g$ values: the shear layer, the upper- and lower flank of the jet. The shear layer has $\hat{R}i_g < 0$ shown in white and $\hat{R}i_g < 0.25$ shown in black. The K-H rollers have a black region surrounded by a white region while the braid is covered in black. At $t = 100$, the upper flank of the jet has $0.25 < \hat{R}i_g < 0.5$ shown in grey, not small enough to support linear instability. In figure 23(b), at $t = 145$, the ‘hot pocket’ marked by a black region below a white region visible at $x = 10\delta_{\omega,0}$ right below the shear layer begins to penetrate the jet. In figure 23(c), at $t = 175$, a large portion of the jet upper flank is covered in black and white, indicating that shear instability is now supported. Energy, indeed, can be extracted from the jet shear at this time.

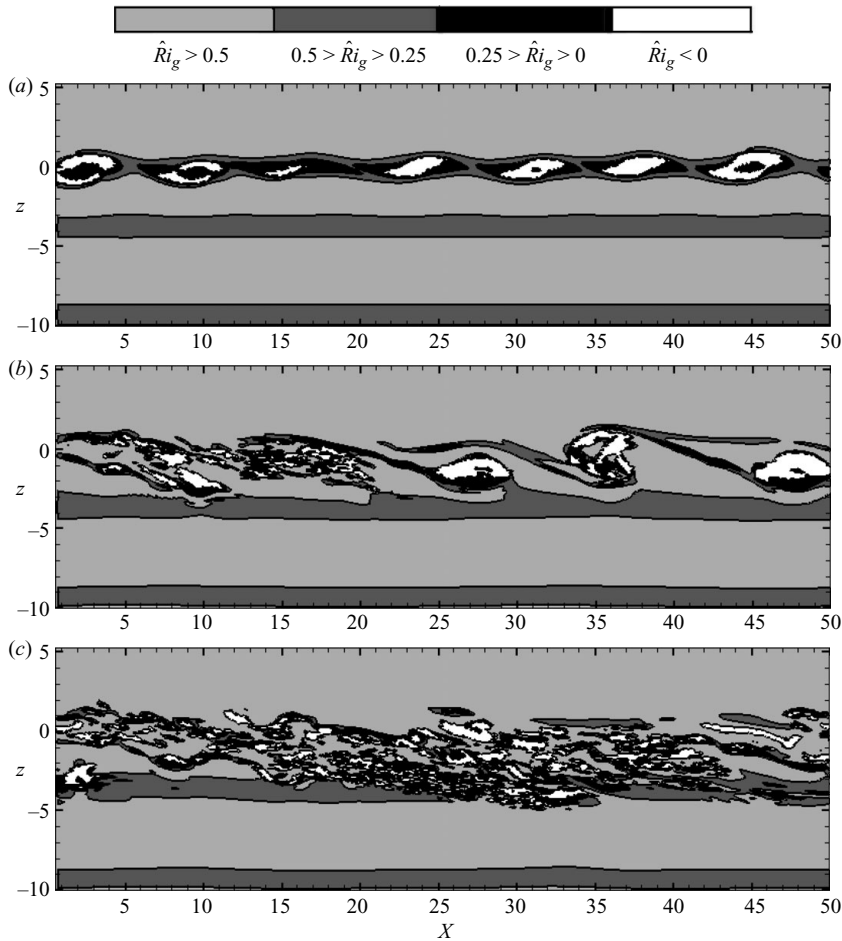


FIGURE 23. Near jet. Local gradient Richardson number \hat{Ri}_g field at $y = 8.4\delta_{\omega,0}$ and $t = 100, 150$ and 170 .

From the discussion in this section, it is evident that the energy feeding into the induced dissipation originates from shear production of TKE. However, it is crucial to distinguish turbulent production from wave production. The time evolution of the integrated production shown in figure 20 indicates that the wave production is significantly less than that in the turbulent production. Using $t = 145$ as a marker that separates the two types of production over the entire simulation, the wave production contributes 17% to the total production while the contribution of turbulent production is 83%.

It is of interest to visually illustrate how the internal waves contribute energy to the induced dissipation. The breakdown of the wave field is shown by the visualization in figure 24, where the vertical scale is increased relative to the horizontal by a factor of 35 to amplify the wave amplitude. The lower four isopycnals in figure 24(a) indicate that the internal waves present in the jet have an approximate wavelength of $25\delta_{\omega,0}$ with the strongest peak-to-trough amplitude of $0.4\delta_{\omega,0}$. The simulated domain contains two wavelengths starting with a crest at the far left and ending with a trough at the far right. The waves are coherent between depths $z = -3\delta_{\omega,0}$ and $z = -5\delta_{\omega,0}$. The ‘hot pocket’ visible at $x = 10\delta_{\omega,0}$ between $-3 < z < -2\delta_{\omega,0}$ causes a distortion of

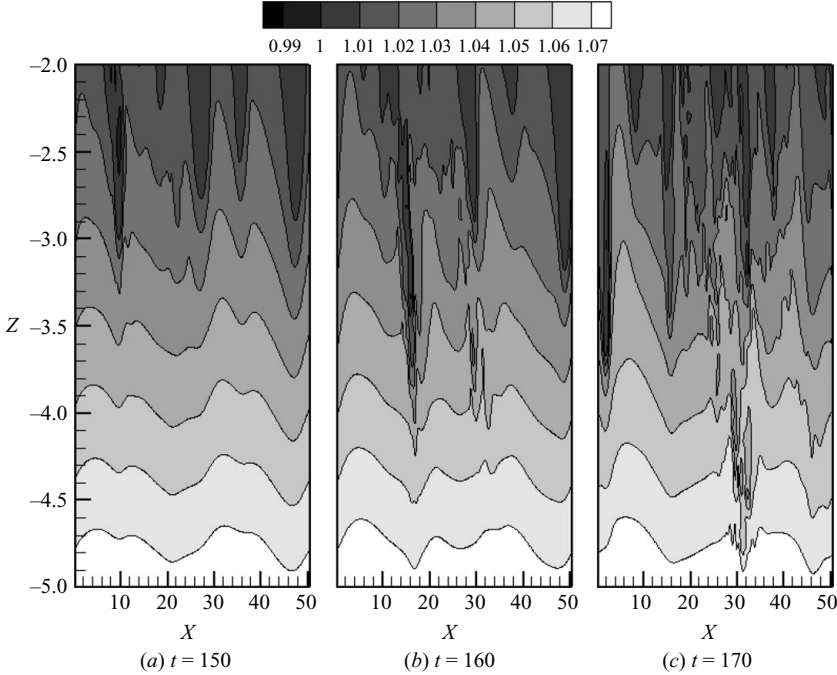


FIGURE 24. Near jet. Expanded view of the density fields with the aspect ratio $L_z:L_x = 1:35$.

the left wave crest increasing its steepness. To assess the impact of $\partial\rho/\partial x$ caused by the penetration of the ‘hot pocket’, it is useful to write an evolution equation for the vertical density gradient. The background shear contributes a term as follows:

$$\frac{D}{Dt} \left(\frac{\partial\rho}{\partial z} \right) \sim - \frac{d\langle u \rangle}{dz} \frac{\partial\rho}{\partial x}. \quad (4.1)$$

According to (4.1), since the background shear is negative, a positive value of $\partial\rho/\partial x$ causes a positive change to the background negative vertical density gradient. Therefore, the local magnitude of stable stratification is reduced and local shear instability is allowed. Figure 24(b) shows the convection of the wave crest in part (a) by the jet velocity. The wave distortion, now at $x \approx 17\delta_{\omega,0}$, intensifies and is surrounded by steep features in the isopycnals. The wave crest is completely digested by strong small-scale fluctuations in figure 24(c), confirming that the nonlinear breakdown of wave energy contributes to the observed dissipation.

It is useful to compare the mixing efficiency between the turbulent patches in the jet and the ones in the shear layer. One way to quantify the mixing efficiency is with the quantity Γ defined as

$$\Gamma(t) = \frac{- \int_V B dz}{\int_V \varepsilon dz}, \quad (4.2)$$

where V is the region of interest. Figure 25(a) shows the evolution of Γ over the time when the turbulent patches in the jet are active. The solid line represents the value of Γ computed by integration over the shear layer with V from $z = -2.5\delta_{\omega,0}$ to z_{max} , while the dashed line corresponds to integration over the jet upper flank,

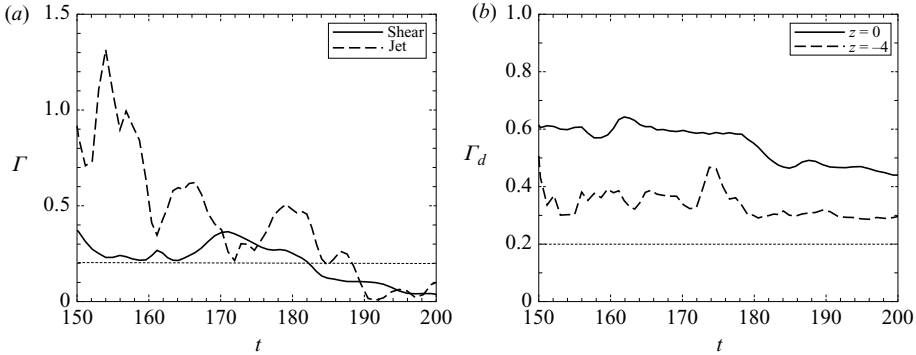


FIGURE 25. Near jet. Mixing efficiency. (a) Γ . (b) Γ_d . The dotted line shows the value of $\Gamma = \Gamma_d = 0.2$.

$-6.5 < z < -2.5\delta_{\omega,0}$. In many oceanic applications, Γ is typically taken to be the constant value of 0.2 (Smyth, Hebert & Moum 1996). In our simulation, Γ is close to this value only in turbulent shear layer. In the jet turbulence, Γ exhibits substantial fluctuations owing to the occasional penetration of the ‘hot pockets’ and is substantially larger than the value of 0.2 during $150 < t < 160$. Later, when turbulence develops and the dissipation rate increases, Γ becomes closer to 0.2. Another measure of mixing is the scalar mixing efficiency, $\Gamma_d(z, t) = \varepsilon/\varepsilon_\rho$, where

$$\varepsilon_\rho(z, t) = \frac{1}{PrRe_0} \frac{g}{\rho_0 |d\bar{\rho}/dz|} \frac{\overline{\partial\rho' \partial\rho'}}{\partial x_k \partial x_k}.$$

Here, ε_ρ denotes the irreversible loss of available turbulent potential energy to the background density. The evolution of Γ_d is shown in figure 25(b) in which the solid and dashed lines indicate the values at $z=0$ and $z=-4\delta_{\omega,0}$, respectively. Γ_d in the shear layer, $z=0$, has a value of approximately 0.6 when $150 < t < 180$. This value is also observed by Smyth, Moum & Caldwell (2001), who characterize mixing efficiency in turbulence patches formed by the breakdown of K-H billows. Γ_d in the turbulent patches in the jet has a smaller value, about 0.4, over the same time period.

5. Conclusions

We have investigated the interaction between an unstable shear layer and a stably stratified ($Ri_g > 0.25$) jet in two situations: a far jet where the distance between the jet and shear layer is large and a near jet where the distance is small relative to the shear-layer thickness. The shape of the mean velocity profile and the Ri_g profile in the near jet case is chosen to be similar to observations in the EUC. Our focus is on the internal wave field and turbulence that ensue in the jet.

In the far case, internal waves with distinct phase lines are excited by K-H rollers and broadband turbulence. The K-H-excited waves follow linear wave theory so that the propagation angle observed in the simulations can be analytically predicted. These waves cannot penetrate the jet and are reflected because the squared vertical wavenumber m^2 in the Taylor–Goldstein (T-G) equation is negative in the jet. There is a build-up of fluctuation kinetic energy in the region between the shear layer and the jet owing to the pressure transport or, equivalently, the internal wave flux. However, there is little turbulence in this region and, consequently, the

turbulent dissipation rate is small, three orders of magnitude below that in the shear layer.

In the near jet, internal waves are also observed but their excitation is not by K-H rollers since the associated value of m^2 in the jet region adjacent to the shear layer is negative. Instead, as the K-H rollers interact nonlinearly and pair, internal waves with smaller wavenumber are excited and found to penetrate the jet since the corresponding $m^2 > 0$. These waves are found to follow linear wave theory as well. There is a region of $m^2 < 0$ in the lower flank of the jet, but the internal waves are able to tunnel through and propagate below the jet. ‘Hot pockets’ of fluid from the upper shear layer are entrained into the stably stratified jet. These pockets are associated with coherent horseshoe vortices that emerge from the unstable shear layer and intensify by interaction with the shear in the stable jet. Coherent patches of small-scale turbulence in the stable jet, initiated by the horseshoe vortices, that are convected by the local mean flow are observed. The dissipation in these patches is comparable to the value observed in the turbulent shear layer and up to three orders of magnitude larger than in the propagating wave field in the far jet case.

The fluctuation field in the stratified near jet consists initially of internal waves. There are a number of changes in the fluctuation field that occur later, immediately after the penetration of hot pockets that signify turbulence: the spectrum of vertical velocity, w , and the co-spectrum of uw change from narrowband with a discrete peak to broadband; the shear production of TKE and the dissipation rate increase sharply; the TKE transport is dominated by turbulent transport instead of the pressure transport (internal wave flux). The local gradient Richardson number based on the local buoyancy frequency and shear becomes subcritical, less than 0.25, showing the potential for shear instability. The terms contributing to the TKE integrated over the upper flank of the stratified jet are evaluated as a function of time. Most of the TKE accumulation in the jet is due to production by the interaction of jet shear with both internal waves and turbulence and not due to the transport term in the TKE equation. Furthermore, the contribution of the wave momentum flux to the shear production of TKE is small (17% of the net shear production) relative to that by turbulence. The counter-gradient heat flux is a source of TKE locally; however, overall, the buoyancy flux is an energy sink.

For the conditions of the model problem, we are able to answer the questions posed in the introduction. (i) Internal waves excited by an unstable shear layer propagate into a stable jet when the jet is near, not when it is far. The presence/absence of internal waves can be predicted by the sign of m^2 in the Taylor–Goldstein equation. (ii) In the near jet, there are patches of significant dissipation with magnitude larger than in the unstable shear layer, although the jet is linearly stable. (iii) The turbulence in the jet is not primarily due to breakdown of the internal wave field.

The simulations suggest that the turbulence observed in our model jet is mainly contributed from local generation of TKE in the jet upper flank where the background shear is marginally stable. Nonetheless, the role of internal waves should not be overlooked in the EUC. In our study, the waves excited by the pairing of the K-H rollers in the *near* jet are significantly weaker than the waves directly excited by the K-H rollers in the *far* jet. The observation of Hebert *et al.* (1992) show large-amplitude internal waves. With a modest variation in either background shear or stratification, the m^2 profile can be changed such that the jet can support K-H-excited waves. Forcing by wind and diurnal heat flux can also force instabilities and energetic waves. Thus, there are situations where the internal wave energy flux can contribute more to the ‘deep-cycle turbulence’ than in the model jet considered here.

A parametric study with systematic variation of background conditions and forcing is necessary to further decipher the complex dynamics of fine-scale fluctuations in the EUC system.

We are grateful for the support provided by ONR N000140710133, program monitor Ron Joslin, and ONR N000140810504, program monitor Scott Harper.

REFERENCES

- BASAK, S. & SARKAR, S. 2006 Dynamics of a stratified shear layer with horizontal shear. *J. Fluid Mech.* **568**, 19–54.
- BROWN, G. L. & SUTHERLAND, B. R. 2007 Internal wave tunnelling through non-uniformly stratified shear flow. *Atmosphere-Ocean* **45**, 47–56.
- BRUCKER, K. & SARKAR, S. 2007 Evolution of an initially turbulent stratified shear layer. *Phys. Fluids* **19**, 101105.
- CAULFIELD, C. P. & PELTIER, W. R. 2000 The anatomy of the mixing transition in homogeneous and stratified free shear layers. *J. Fluid Mech.* **413**, 1–47.
- GREGG, M. C., PETERS, H., WESSON, J. C., OAKEY, N. S. & SHAY, T. J. 1985 Intensive measurements of turbulence and shear in the equatorial undercurrent. *Nature* **314** (14), 140–144.
- HEBERT, D., MOUM, J., PAULSON, C. & CALDWELL, D. 1992 Turbulence and internal waves at the equator. Part ii. Details of a single event. *J. Phys. Oceanogr.* **22**, 1346–1356.
- JEONG, J. & HUSSAIN, F. 1995 On the identification of a vortex. *J. Fluid Mech.* **285**, 64–94.
- KOOP, C. G. & BROWAND, F. K. 1979 Instability and turbulence in a stratified fluid with shear. *J. Fluid Mech.* **93**, 135–159.
- LIEN, R.-C., MCPHADEN, M. & GREGG, M. 1996 High-frequency internal waves at 0°, 140° w and their possible relationship to deep-cycle turbulence. *J. Phys. Oceanogr.* **26**, 581–600.
- MAHALOV, A., MOUSTAOU, M., NICOLAENKO, B. & TSE, K. L. 2007 Computational studies of inertia-gravity waves radiated from upper tropospheric jets. *Theoret. Comput. Fluid Dyn.* **21**, 399–422.
- MOUM, J., HEBERT, D., PAULSON, C. & CALDWELL, D. 1992 Turbulence and internal waves at the equator. Part i: Statistics from towed thermistors and a microstructure profiler. *J. Phys. Oceanogr.* **22**, 1330–1345.
- PETERS, H., GREGG, M. & TOOLE, J. 1988 On the parameterization of equatorial turbulence. *J. Geophys. Res.* **93** (C2), 1199–1218.
- PHAM, H. T., SARKAR, S. & BRUCKER, K. A. 2009 Dynamics of a stratified shear layer above a region of uniform stratification. *J. Fluid Mech.* **630**, 191–223.
- SKYLLINGSTAD, E. & DENBO, D. 1994 The role of internal gravity waves in the equatorial current system. *J. Phys. Oceanogr.* **24**, 2093–2110.
- SMYTH, W. D., HEBERT, D. & MOUM, J. N. 1996 Local ocean response to a multiphase westerly wind burst. Part 2. Thermal and fresh water responses. *J. Geophys. Res.* **101** (C10), 22513–22533.
- SMYTH, W. D. & MOUM, J. N. 2000 Anisotropy of turbulence in stably stratified mixing layers. *Phys. Fluids* **12** (6), 1343–1362.
- SMYTH, W. & MOUM, J. 2002 Shear instability and gravity wave saturation in an asymmetrically stratified jet. *Dyn. Atmos. Oceans* **35**, 265–294.
- SMYTH, W. D., MOUM, J. N. & CALDWELL, D. R. 2001 The efficiency of mixing in turbulent patches: inferences from direct simulations and microstructure observations. *J. Phys. Oceanogr.* **31**, 1969–1992.
- STRANG, E. J. & FERNANDO, H. J. S. 2001 Entrainment and mixing in stratified shear flows. *J. Fluid Mech.* **428**, 349–386.
- SUN, C., SMYTH, W. & MOUM, J. 1998 Dynamic instability of stratified shear flow in the upper equatorial pacific. *J. Geophys. Res.* **103**, 10323–10337.
- SUTHERLAND, B. & LINDEN, P. 1998 Internal wave excitation from stratified flow over thin barrier. *J. Fluid Mech.* **377**, 223–252.
- SUTHERLAND, B. R. 2006 Rayleigh wave-internal wave coupling and internal wave generation above a model jet stream. *J. Atmos. Sci.* **63**, 1042–1055.

- SUTHERLAND, B. R. & PELTIER, W. 1992 The stability of stratified jets. *Geophys. Astrophys. Fluid Dyn.* **66**, 101–131.
- THORPE, S. A. 1973 Experiments on instability and turbulence in a stratified shear flow. *J. Fluid Mech.* **61**, 731–751.
- TSE, K. L., MAHALOV, A., NICOLAENKO, B. & FERNANDO, H. J. S. 2003 Quasi-equilibrium dynamics of shear-stratified turbulence in a model tropospheric jet. *J. Fluid Mech.* **496**, 73–103.
- WINTERS, K. B. & D'ASARO, E. A. 1994 Three-dimensional wave instability near a critical layer. *J. Fluid Mech.* **272**, 255–284.